MATERIALS SCIENCE

Designing hierarchical nanoporous membranes for highly efficient gas adsorption and storage

Haiyan Mao[1]*, Jing Tang[2,3]*, Jun Chen[2], Jiayu Wan[2], Kaipeng Hou[1], Yucan Peng[2], David M. Halat[1,4], Liangang Xiao[4], Rufan Zhang[2], Xudong Lv[1], Ankun Yang[2], Yi Cui[2,3]†, Jeffrey A. Reimer[1,4]†

Nanoporous membranes with two-dimensional materials such as graphene oxide have attracted attention in volatile organic compounds (VOCs) and H_2 adsorption because of their unique molecular sieving properties and operational simplicity. However, agglomeration of graphene sheets and low efficiency remain challenging. Therefore, we designed hierarchical nanoporous membranes (HNMs), a class of nanocomposites combined with a carbon sphere and graphene oxide. Hierarchical carbon spheres, prepared following Murray's law using chemical activation incorporating microwave heating, act as spacers and adsorbents. Hierarchical carbon spheres preclude the agglomeration of graphene oxide, while graphene oxide sheets physically disperse, ensuring structural stability. The obtained HNMs contain micropores that are dominated by a combination of ultramicropores and mesopores, resulting in high VOCs/H_2 adsorption capacity, up to 235 and 352 mg/g at 200 ppmv and 3.3 weight % (77 K and 1.2 bar), respectively. Our work substantially expands the potential for HNMs applications in the environmental and energy fields.

INTRODUCTION

The design of materials for gas separation and storage is challenging due to a number of ostensibly conflicting goals (*1*). Pores on the order of molecular dimensions are deemed necessary for discrimination of various gases on the basis of size, yet they must be chemically functionalized to afford chemical selectivity in the adsorption process (*2*). Narrow pores limit the transport of gases required for large-scale processing of gases and molecular-sized pores. Moreover, owing to capillary effects, narrow pores are prone to clogging with impurities or condensation of gases (*3*). Polymer membranes, so profoundly effective in large-scale separations, are limited by the Robeson criteria, where the solubility-diffusion protocol relies on crafted polymer-free volume (*4*). These challenges motivate the design of hierarchically structured membrane materials, that ameliorate these challenges. In the present work, we create these hierarchical materials by combining elegant two-dimensional (2D) nanosheets with sustainably synthesized carbon spheres so as to produce a "meatball sandwich" via an easily scaled production process. We demonstrate these hierarchically structured materials can undergo volatile organic adsorption and hydrogen gas storage.

Industrial gas separations and storage have a long history, where porous materials, such as activated carbons, zeolites, and metal-organic frameworks (MOFs), have been used for the removal of volatile organic compounds (VOCs) and the storage of H_2 (*5*, *6*). Partly owing to their expense of production, activated carbon and zeolite membranes promise capacities of 3.0 to 5.5 weight % (wt %) at 79 atm and 298 K for H_2 and 300 to 650 mg/g at 1 atm and 298 K for the prototypical VOC toluene (*7*). Limited mechanical stability, however, restricts their applications: activated carbon membranes are very brittle and fragile. Compared with other conventional adsorbents, the merits of MOF membranes are their large surface areas, rich functionalities, and targeted synthesis, resulting in capacities of 1.1 wt % for H_2 and 276 mg/g for toluene at 1 atm and 298 K (*5*, *6*). Some MOF membranes exhibit high gas adsorption performance; however, their large-area production is associated with increased fragility and cracks (*5*).

Recently, nanoporous inorganic membranes with 2D materials [e.g., graphene oxide (GO)] have been shown to exhibit high surface areas, ultralight weights, and high adsorption capacities, thereby attracting immense interest in electrochemical energy storage and water purification (*7*–*9*). Nevertheless, GO membranes are very difficult to handle and are expensive to process into membrane configurations (e.g., multilayered stacks and mixed-matrix membranes) (*10*, *11*). In particular, the facile aggregation (Fig. 1A) of graphene sheets leads to a distinct decrease in accessible surface area for gases (e.g., VOC and H_2) and a notable increase in molecular diffusion resistance that deleteriously affects adsorption performance (*12*).

Carbon spheres with hierarchical micro- and mesopores have drawn considerable attention in applications for VOC and H_2 adsorption due to their high sphericity, high selectivity, and high porosity. These spheres may be constructed into membranes (Fig. 1B) via the use of binders, yet these membranes are susceptible to mechanical instability, high manufacturing cost, and the clogging of the binders added to form the membranes (*2*). We surmised that hierarchical nanoporous membranes (HNMs) structures (Fig. 1C) could be assembled wherein carbon spheres serve as effective "nanoporous spacers" and substantially improve cross-plane mass transfer via expanded interlayer spacing, while the agglomeration and stacking of spheres are alleviated via the use of pure GO membranes (*13*) that bind strongly to the spheres. In imagining this construct, we were mindful that these carbon spheres must present an array of pore sizes, such as the "Murray's law" (*14*) hierarchy, and could be derived and processed sustainably. We chose to use a crafted hydrothermal carbonization of pinewood-based cellulose and chemical activation

[1]Department of Chemical and Biomolecular Engineering, Department of Chemistry, University of California, Berkeley, Berkeley, CA 94720, USA. [2]Department of Materials Science and Engineering, Stanford University, Stanford, CA 94305, USA. [3]Stanford Institute for Materials and Energy Sciences, SLAC National Accelerator Laboratory, 2575 S and Hill Road, Menlo Park, CA 94025, USA. [4]Materials Science Division, Lawrence Berkeley National Lab, Berkeley, CA 94720, USA.
*These authors contributed equally to this work.
†Corresponding author. Email: yicui@stanford.edu (Y.C.); reimer@berkeley.edu (J.A.R.)

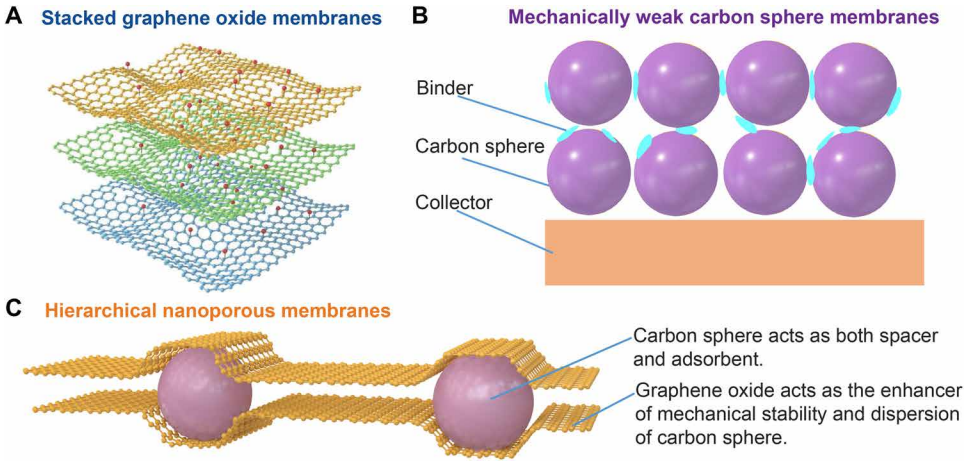

Fig. 1. Comparison of a schematic illustration of GO membranes, carbon sphere membranes, and HNMs. (**A**) Designed structural model of stacked graphene membranes. (**B**) Model of mechanically weak layers of carbon sphere membranes by binders. (**C**) Model of the mechanical strength and high adsorption capacity of HNMs. As a comparison of GO membranes and carbon sphere membranes, our HNMs combined the merits of both GO and carbon sphere membranes: In this meatball sandwich structure, carbon spheres act as spacers and adsorbents, precluding the agglomeration of GO. GO sheets physically disperse carbon spheres, ensuring mechanical stability.

to produce Murray's law spheres that, when mixed with GO, could be fashioned into membranes using an extremely simple "doctor-blade" method. The obtained porous HNMs are dominated by a combination of micropores and mesopores, resulting in high toluene/H_2 adsorption capacity up to 235 and 352 mg/g at 200 parts per million by volume (ppmv) and 3.3 wt % (77 K and 1.2 bar), respectively.

RESULTS AND DISCUSSION

Fabrication and structural characterization of carbon spheres

Fabricating the hierarchical carbon spheres (HCSs) with high surface area, high sphericity, and monodispersibility requires several key steps, including hydrothermal carbonization synthesis (Fig. 2A) and chemical-microwave activation procedures (Fig. 2B) to be discussed later. The effects of the reaction temperature, reaction time, and cellulose concentration on the morphology by scanning electron microscopy (SEM) of the HCSs via hydrothermal carbonization synthesis were investigated and are discussed in the Supplementary Materials (figs. S1 to S3). We find that when the hydrothermal temperature increases from 200° to 240°C, cellulose decomposes rapidly, and hydrothermal carbons with a higher degree of aromatization are generated (*15*). The resulting particles also exhibit a more uniform size. Accordingly, we surmise that the aromatization reaction occurred with dehydrogenation of cellulose at 240°C, and the resulting hydrothermal products had a high degree of sphericity, narrow distribution of particle size, and an average diameter of approximately 3 μm. However, aggregation emerges among carbon spheres when the temperature rises to 260°C (fig. S1C). The longer reaction time yields larger particle size and gives rise to particles with irregular shapes. When the reaction time increases from 5 to 7 hours, wood cellulose is deposited at the bottom of the reaction vessel, resulting in a relatively large concentration of carbon spheres at the bottom (fig. S2B). When the concentration of cellulose is increased from 0.02 (fig. S3A) to 0.04 g ml^{-1} (Fig. 2E), the diameter of the HCS increases. However, when the concentration of cellulose reaches a certain threshold, the size becomes constant (*16*). We further find

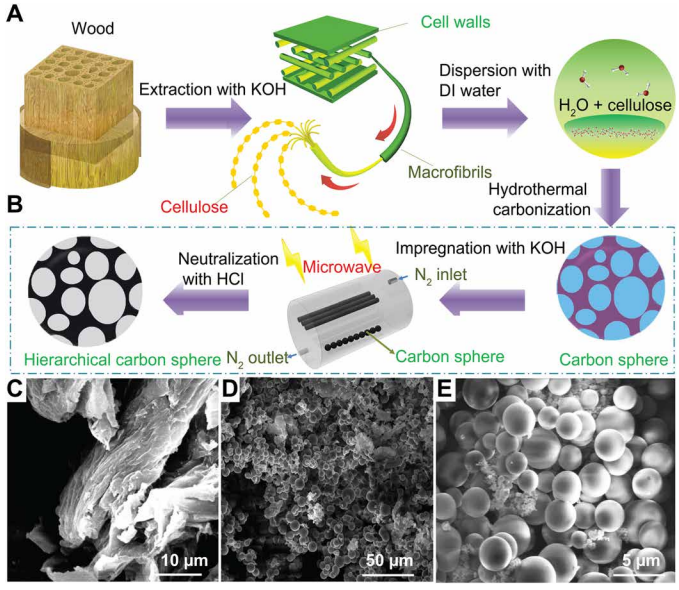

Fig. 2. Wood-derived HCS. (**A**) Schematic diagram of the fabrication process of the carbon sphere. (**B**) Schematic diagram of the fabrication process of the HCS. (**C** to **E**) SEM images of cellulose and the carbon spheres.

that the diameter of a few individual carbon spheres tends to decrease when the concentration reaches 0.05 g ml^{-1} (fig. S3C). We conclude that the optimized hydrothermal products result from conditions of 240°C for 5 hours with a reaction concentration of 0.04 g ml^{-1}. Figure 2C shows SEM images of the original cellulose. After our optimal treatment, Fig. 2 (D and E) shows the SEM images of the optimal carbon spheres, demonstrating spherical morphology, with an average diameter of 2 to 3 μm. It was also confirmed that the carbon spheres have a smooth surface without a hollow interior.

Figure 3A shows the infrared (IR) spectra of cellulose and carbon spheres prepared from cellulose at 240°C by hydrothermal carbonization for 5 hours with a concentration of 0.04 g ml^{-1}.

For the IR spectrum of the carbon spheres, the peak at 1702 cm^{-1} corresponds to the stretching vibration of the C═O of carbonyl, quinone, ester, or carboxyl (*17*). The peak at 1024 cm^{-1} is due to the O─H bending vibration. These results indicate that a large number of oxygen functional groups (C═O and OH) are present on the surface of the HCS. The vibration of carbon-carbon double bonds produces a vibrational band at 1612 cm^{-1}. The out-of-plane bending vibrations of C─H bonds of aromatic rings lead to a vibrational band at 875 to 750 cm^{-1}, demonstrating the presence of aromatic rings in the product (*18*). In addition, the peak at 2925 cm^{-1} corresponds to the stretching vibration of C─H, demonstrating the presence of aliphatic structures and aromatization during the reaction. A comparison of the changes in the cellulose and carbon sphere spectra suggests that cellulose undergoes dehydration and aromatization reactions in the process of hydrothermal carbonization. In addition, the surfaces of the carbon spheres contain large amounts of oxygen functional groups, including C═O and OH.

The crystalline or amorphous structure of the cellulose and carbon spheres was investigated by x-ray diffraction (XRD) analysis (*18*, *19*). Figure 3B shows the XRD patterns of cellulose and carbon spheres obtained from optimal conditions. Distinct diffraction peaks for cellulose appear at 2θ = 16°, 23°, and 34°, corresponding to the (101), (002), and (040) crystal planes, respectively (Fig. 3B). To some extent, these features indicate that the cellulose exhibits crystallinity to some extent (*19*). Figure 3B reveals that at 240°C, the cellulose-based products undergo a hydrothermal reaction. As a result, the diffraction peaks for the (101) and (040) planes disappear, and the (002) peak at 2θ = 23° becomes flat, indicating that the hydrothermal reaction at 240°C destroys the internal structure of the cellulose during carbonization. Thus, the resulting carbon materials exist in an amorphous state.

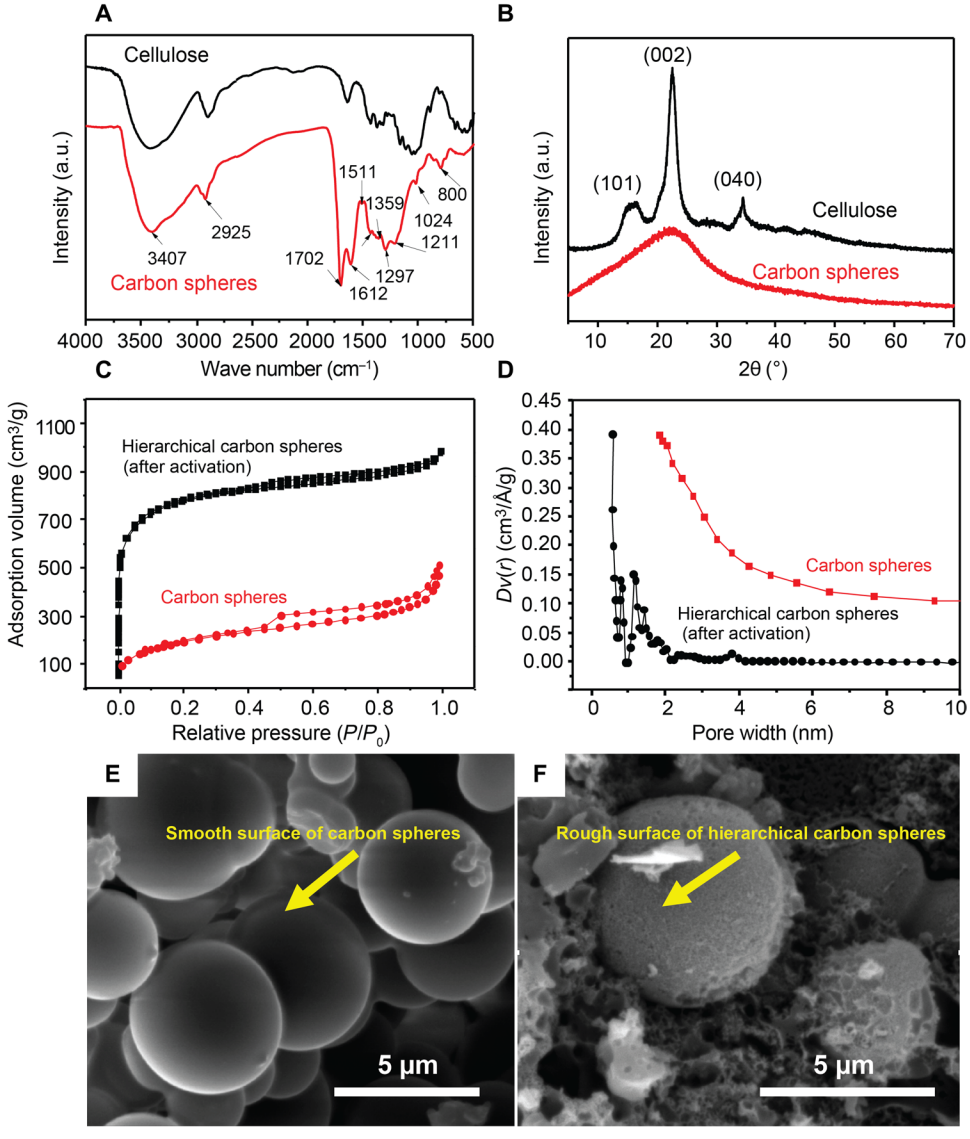

Fig. 3. Characterization of carbon spheres and HCSs. (**A**) FTIR spectra of the original cellulose and HCSs after hydrothermal treatment of 0.04 g ml^{-1} at 240°C for 5 hours. (**B**) XRD patterns of the original cellulose and carbon spheres after the same hydrothermal treatment. (**C** and **D**) N_2 adsorption isotherms at 77 K and pore size distribution. (**E** and **F**) SEM images of carbon spheres and HCSs. After activation by KOH and microwave heating, HCSs exhibit a majority of micropores and a small number of meso-macropores (C and F), which are beneficial for VOC adsorption and diffusion within HCSs. a.u., arbitrary units.

Tunable porous structure of HCSs

With natural cellulose derived from woodchips as the starting material, we deployed a facile approach of hydrothermal carbonization by incorporating KOH and microwave heating activation, as described previously (Fig. 2B). Figure 3C shows the low-temperature nitrogen adsorption isotherms of carbon spheres and HCSs samples produced by a combination of KOH and microwave heating. According to the Brunauer-Deming-Deming-Teller (BDDT) classification (*20*), the carbon sphere isotherm can be assigned to hybrid types I to IV, in which increased relative pressure (P/P_0) leads to a small increase in adsorption. A hysteresis loop is formed and associated with capillary condensation taking place in the mesopores and limits uptake of gas over a range of high P/P_0. After activation, the adsorption isotherms of the HCS are still hybrid types I to IV. The initial adsorption and flatter plateau regions at higher relative pressures imply that micropores dominate in HCS. However, the adsorption curve is not horizontal, but sloped. The desorption curve shows hysteresis when the relative pressure is greater than 0.2, indicating that the HCSs have a wide pore size distribution because the samples contain a small number of mesopores and macropores. Micropore filling mainly occurs at the beginning of the isotherm. When the relative pressure increases, multilayer adsorption occurs, followed by capillary condensation at higher partial pressures (*21*). Therefore, the adsorption capacity increases with relative pressure.

The pore size distribution of the carbon spheres suggests a mesoporous structure before activation, as shown in Fig. 3D. After activation, the distribution peaks of the curves of the HCSs are distinctly visible between 0.5 and 1 nm on the abscissa. Most of the pores in the HCSs are less than 2 nm, but a small portion of the HCS have a pore size less than 0.7 nm, indicating that the HCSs formed via KOH and microwave activation are mainly characterized by micropores but contain a considerable number of ultramicropores, supermicropores and a small number of mesopores. The magnified inset in Fig. 3D shows that the number of ultramicropores in the sample of HCS increases slightly after KOH activation. Therefore, activated HCSs are suitable for gas adsorption, such as the adsorption of VOCs or H_2.

On the basis of the adsorption isotherms, table S1 lists the structural parameters of the HCS before and after activation, including the Brunauer-Emmett-Teller (BET) (*22*) surface area (S_p), micropore area (S_{micro}), total pore volume (V_{pore}), and micropore volume (V_{micro}). The surface area of the HCS increases from 528 to 2551 m^2/g after KOH and microwave heating. V_{micro} and V_{pore} also show the same trend, increasing from 0.016 and 0.120 cm^3/g to 0.796 and 0.916 cm^3/g, respectively. This trend is mainly due to the impregnation of the material with KOH; the KOH molecules continuously permeate from the exterior of the carbon spheres into the interior via microwave heating, and as the reaction between KOH and C increases, a greater number of micropores is formed. In addition, the pore structure of the carbon spheres facilitates the penetration of KOH molecules, and more micropores are developed rapidly.

The SEM images of KOH and microwave-treated HCSs (Fig. 3, E and F) further confirm the effects of these methods on carbon spheres. Compared with carbon spheres (Fig. 3E), the surface of HCS shows obvious roughening, which indicates that the etching of micropores can be achieved within a short microwave irradiation period. Therefore, HCSs display combined micro-mesoporous structures expected to enhance the VOC adsorption performance. In addition, abundant mesopores and small micropores in the original carbon sphere walls generated by the activation treatment are consistent with a large microporous surface area; moreover, small mesopores also provide pathways for VOCs/H_2 through the porous particles. The combined meso-micropore hierarchical structure of the carbon spheres can substantially contribute to the high VOC/H_2 adsorption capacity.

Fabrication and characterization of GO/HCS composites

The GO/HCS composites were synthesized using the method shown in Fig. 4A and were investigated by SEM, with the images shown in Fig. 4 (B and C). It is apparent that the GO/HCS composite is composed of two components, carbon spheres and GO (Fig. 4B). Carbon spheres were well distributed as barriers to separate the graphene nanosheets, as seen from the SEM pictures (Fig. 4, B and C), and this result is in good agreement with previous work (*23*). Moreover, the HCSs retain a spherical morphology without obvious damage or wrinkled textures following GO coating on the surface of the HCS. The present GO/HCS composites are preferable to the previously reported polydopamine sphere/GO composites, which showed wrinkled carbon spheres after GO coating (*13*). The current results reveal that KOH-activated cellulose-based carbon spheres can effectively prevent graphene aggregation and lead to the successful fabrication of novel GO/HCS composites.

Fabrication and structural characterization of HNM

We deploy a scalable approach to fabricate HNM using a doctor-blade deposition technique, as shown in Fig. 5A. Our designed doctor-blade method shows the advantages of highly versatile, uniform, and freestanding membranes with a precisely controlled thickness (*24*). Figure 5B shows freestanding and flexible HNM. HNMs show a greater degree of corrugation compared to pure GOs due either to the development of hierarchical pores or to defects on the sheets, which is assumed to be beneficial for VOC diffusion and adsorption. Figure 5 (C to F) provides images of the top view of the surface of the membranes, revealing that the HCSs are wrapped with GO and retain a spherical morphology. Cross-sectional high-resolution SEM images of the edge of the GO/HCS membranes show that the HCSs act as spacers preventing the restacking of the sheets (Fig. 5, G and H), with a membrane thickness of 20 μm. Meanwhile, GO appears to induce the separation of the HCS and prevents the aggregation of carbon spheres.

Raman spectra of the HNM, as well as the GO and the HCS, are shown in Fig. 5I. As expected, two peaks are detected at 1328 cm^{-1} (D band) and 1589 cm^{-1} (G band), confirming the successful loading of the GO. Similar peaks, which were found for the GO and carbon sphere composite, were attributed to an increase in the sp^2 carbon network (*23*). As is well known, defects and disorder within wood-derived carbon materials lead to an increase in the intensity of the D band, while the in-plane stretching of sp^2-bonded carbon (i.e., nondefective sites) corresponds to the G band (*18*). The extent of structural defects in the samples is shown by the value of the intensity of the [D] (I_D) band relative to that of the [G] (I_G) band. The ratios of I_D and I_G values (I_D/I_G) for the HNM, GO, and HCS are 1.21, 0.89, and 0.32, respectively. The I_D/I_G value for the GO/HCS has slightly increased compared with the GO, implying that GO becomes disordered after the HCS undergoes insertion into the interlayers of GO. The introduction of more sp^3 defects in HNM resulted in a larger surface area, which favors gas adsorption and transportation. It is important to note that our HNMs have great potential to

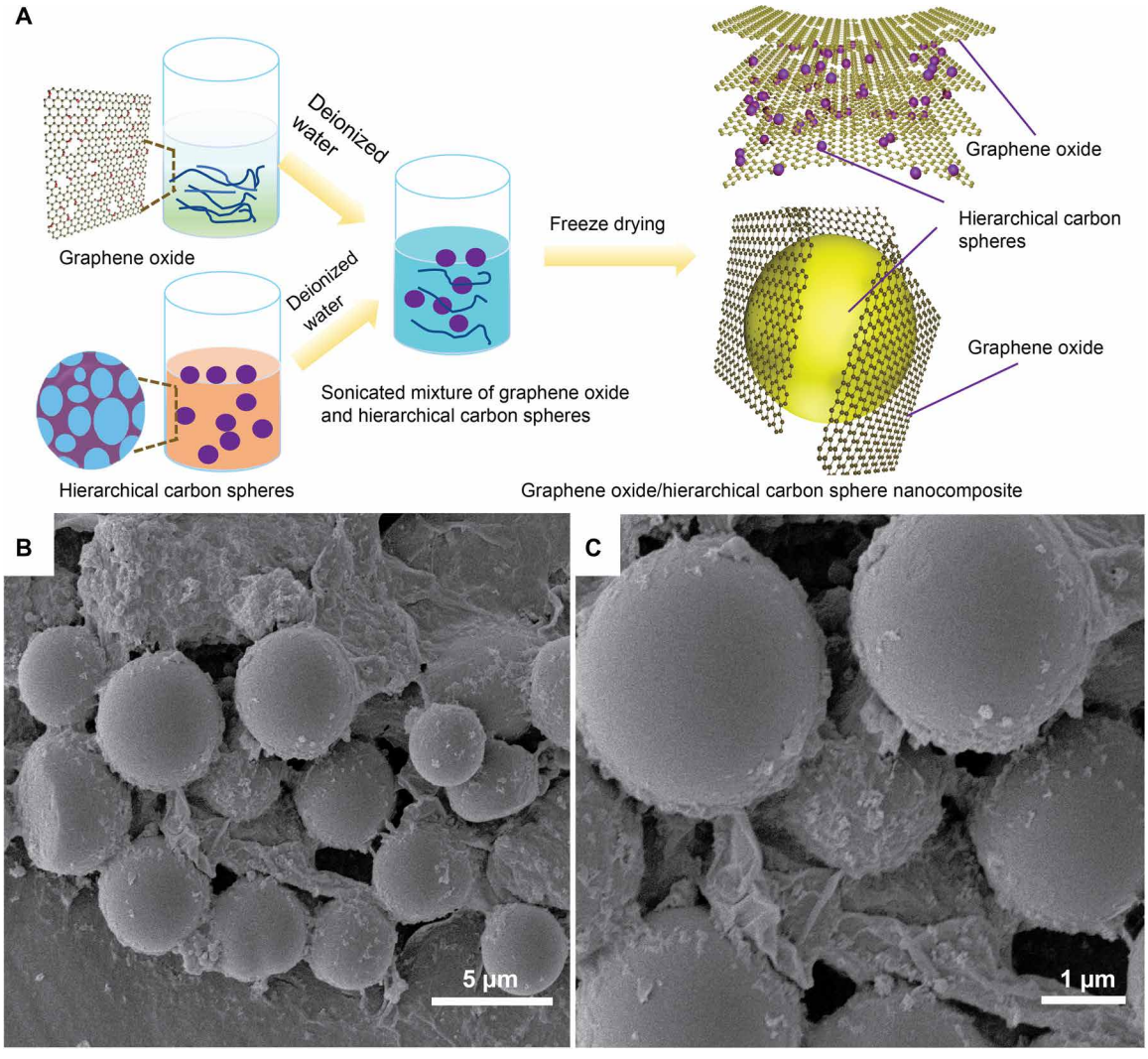

Fig. 4. Schematic diagram and SEM images of GO/HCS nanocomposite. (**A**) Schematic diagram of GO/HCS nanocomposite preparation. (**B** and **C**) SEM images of GO/HCS nanocomposite.

be easily scaled up (Fig. 5B and fig. S4A), as the doctor-blade coating method has no fundamental limitation to prepare meter-scale HCSs and GO membranes. Figure S4B shows the excellent flexibility and mechanical strength in HNM due to the flexible and freestanding GO, allowing them to endure deformations without affecting their structural integrity. All of the present evidence confirms the facile fabrication procedure, large surface area, low cost of the starting materials, and easy up-scaling making HNM the most promising candidate for VOC adsorption and H_2 storage.

VOC adsorption performance of HNM

Adsorption performance of VOCs can elucidate the contribution of the hierarchical structure and mechanical stability of HNM. A sorption analyzer was used to measure the adsorption isotherms of toluene and acetone at 25°C, as shown in Fig. 6 (C and D). The HNMs obtained in this study show high adsorption performance for toluene and acetone, with adsorption capacities as high as 760 and 552 mg/g, respectively. The adsorption capacities are comparable to other porous materials (*25*–*28*). The adsorption isotherms show behavior corresponding to type I adsorbents. All adsorption isotherms exhibit the same trend, with the curves increasing at a relative pressure of 0 to 0.1. With the increase in relative pressure, the adsorption isotherm approaches or approximates a horizontal asymptote, suggesting that the pore structure is mainly composed of micropores (*28*). That is, the adsorption capacity slowly increases at high concentrations, and the slope of the adsorption isotherm gradually decreases and then becomes flat. Although, at low concentrations, there is only a small difference in concentration between the interior and exterior of the micropores in the HNM, the micropores are extremely well developed and can efficiently adsorb toluene/acetone molecules, resulting in a rapid increase in the adsorption capacity (*29*). Furthermore although the difference in the adsorbent concentration between the interior and exterior of the micropores is small at the concentrations, the micropores gradually become saturated because of limitations in the adsorption capacity of the HNM. Therefore, the adsorption of VOCs slowly increases and tends to become constant. The Dubinin-Radushkevich (D-R) equation (*30*) was adopted to fit the corresponding isotherms; as shown, the

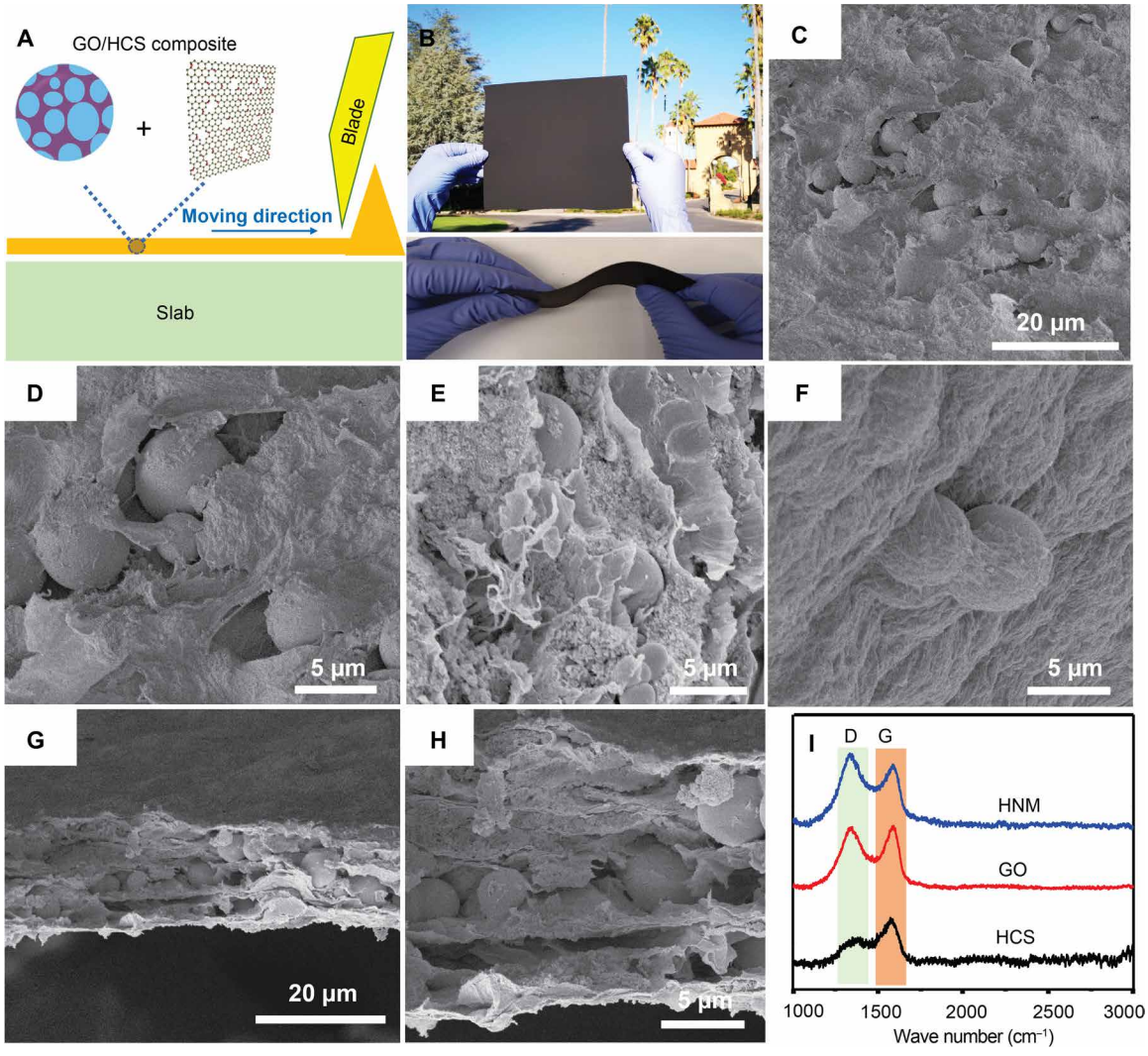

Fig. 5. Doctor-blade coating technique to fabricate HNM. (**A**) Schematic illustration of the blade-coating method for forming HNM. (**B**) Photographs of a large-area HNM (10 cm by 10 cm) fabricated by the doctor-blade method. (**C** to **F**) SEM images of HNM. (**G** and **H**) SEM images of cross-sectional edge of HNM. (**I**) Raman spectra of HCS, GO, and HNM. The D band corresponds to the defects and disorder within the wood-derived carbon, while the G band is due to the in-plane stretching of sp^2-bonded carbon. Photo credit: J.T., Stanford University. Permission granted.

two isotherms fit the D-R equation well (fit parameters are given in table S2).

We measured t dynamic adsorption breakthrough curves of the HNM loaded with toluene and acetone at 200 ppmv, using the experimental apparatus shown in Fig. 6A. A structural model of the proposed toluene and acetone adsorption mechanism in the HNM is also depicted (Fig. 6B). The adsorption penetration results are shown in Fig. 6E; the adsorption breakthrough times of the HNM were approximately 4.5 and 6 hours for acetone and toluene, respectively. All the adsorption breakthrough curves require a long time to saturate, illustrating a large mass transfer resistance likely due to the narrow micropore entrance within the microporous-dominated membranes yielding a low diffusion rate (*31*). A longer breakthrough time indicates a better adsorption capacity for a constant concentration. The saturated acetone and toluene adsorption capacity reached 235 and 352 mg/g, respectively, which are both higher than those of commercial activated carbons (121 and 188 mg/g for acetone and toluene, respectively) (Fig. 6F). This result suggests that our HNMs show promising adsorption performance in low-concentration VOC environments.

HNM for H_2 storage

The exceptionally high surface areas, along with the hierarchical micropore-dominated structures, make HNM very attractive candidates for hydrogen storage. As indicated in Fig. 6 (G and H), the highest adsorption amount of H_2 at 77 K and 1.2 bar for HNM is up to 3.3 wt %. These H_2 adsorption uptakes are competitive with those of other porous materials, such as activated carbons (1.4 to 1.6 wt % at 77 K and 1 bar; 6.6 wt % at 77 K and 4 MPa) (*32*) and MOFs (0.7 to 2.5 wt % at 77 K and 1 bar) (*33*). Thus, HNMs present advantages for hydrogen adsorption such as low cost, good reversibility, and safety. The cost-effectiveness and durability of HNM were demonstrated by the reusability over multiple adsorption-desorption cycles in fig. S5 and table S3, which show the VOC adsorption capacities

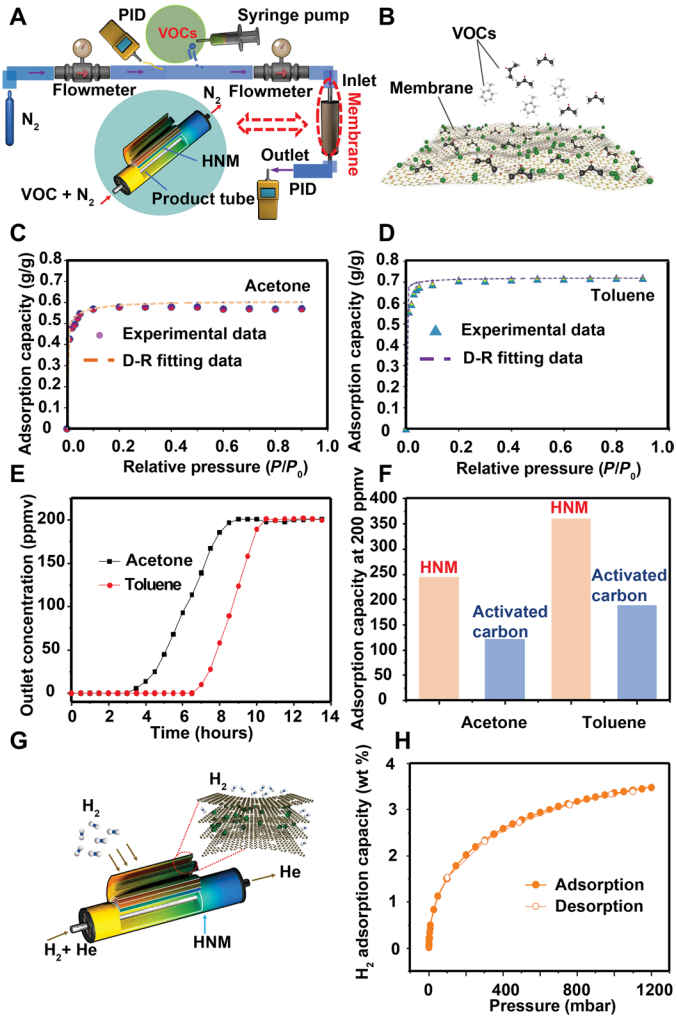

Fig. 6. VOC and H_2 adsorption performance of HNM. (**A**) Schematic diagram of experimental setup for measuring VOC adsorption. (**B**) Structural model for toluene and acetone adsorption. (**C** and **D**) Acetone and toluene adsorption isotherms and D-R fitting. (**E**) Breakthrough curves for acetone and toluene at 200 ppmv. (**F**) Adsorption capacities of HNM and activated carbons at the outlet concentration of 200 ppmv. (**G**) Schematic diagram of H_2 adsorption. (**H**) Equilibrium H_2 adsorption isotherms at 77 K.

and yields of HNM over five cycles by repetitive thermal heating. The efficiency could be sustained up to 98.5% over five cycles, demonstrating that our HNMs have effective desorption after thermal heating with repeated cycling. This cyclability and high adsorption performance, combined with the economics, durability, and ease of scaling, confirm the cost-effective utilization of the membranes.

MATERIALS AND METHODS

Materials and chemicals

Wood cellulose was extracted from pinewood using an alkaline aqueous solution (KOH). A 3% potassium hydroxide solution was obtained by mixing potassium hydroxide powder (Sigma-Aldrich) and deionized (DI) water at the appropriate mass ratio. A 2% dilute sulfuric acid solution was obtained by adding 98% sulfuric acid (Sigma-Aldrich) to DI water at the appropriate volumetric ratio. Commercial activated carbon derived from biomass was used in the study as a comparison at 200 ppmv of acetone and toluene (Sigma-Aldrich). The initial mixing was conducted at room temperature. Afterward, the mixture was placed on a hot plate stirrer and held at approximately 80°C and then transferred to a constant-temperature drying oven (held at 60°C) to prevent the formation of mildew caused by the water content in the purified microcrystalline cellulose, before the hydrothermal carbonization step.

Synthesis of wood cellulose–based carbon spheres

To prepare carbon spheres, 0.3, 0.4, 0.5, 0.6, and 0.8 g of wood cellulose were weighed and placed into sample bottles, and 15 ml of DI water was added; the mixture was stirred for 30 min at 30 rpm to disperse the cellulose uniformly. Then, the solution was placed into a hydrothermal reaction vessel, sealed, placed in a muffle furnace, and held for 3, 5, or 7 hours at a constant temperature of 200°, 220°, 240°, or 260°C. Then, the solution was naturally cooled to room temperature in the muffle furnace. The substance in the lower layer of the hydrothermal reaction vessel was subjected to suction filtration, washed with ethyl alcohol and DI water, and dried at 100°C for 12 hours.

Microwave and KOH activation of carbon spheres

A total of 3 g of dried carbon spheres was weighed and placed into a beaker. Then, 7.5 g of KOH was weighed (corresponding to the impregnation ratio KOH/C = 2.5) and dissolved in DI water. The weighed charcoal was placed into the KOH solution, impregnated for 24 hours, and then dried for 12 hours in an oven at 120°C. After the charcoal with the KOH solution had completely dried, the impregnated carbon was weighed, and the yield was calculated. The carbon spheres were placed in a 50-ml crucible, which were put into a quartz glass beaker. Then, the beaker with carbon spheres was placed in a microwave oven for activation for 30 min (Fig. 2B). The microwave oven was connected to a gas line before it was fed with nitrogen. After the oxygen in the beaker was removed, the microwave irradiation period was set to 10 min, and the power was set to 700 W. After finishing the activation, the HCSs were neutralized using 0.1 M hydrochloric acid, and the material was impregnated for 1 hour. After the remaining KOH was entirely removed from the pores and neutralized, the HCSs were washed with water and put into the oven at 120°C for 24 hours. The neutralized HCSs were ready for use after the drying was completed.

Preparation of GO/activated HCS composite

GO was prepared by the modified Hummers method, as reported previously (*34*). GO (0.5 g) was dispersed in 200 ml of DI water and sonicated for 4 hours. Next, 0.5 g of HCS was added into the GO dispersion and stirred for 24 hours. The product was then washed with DI water several times and finally freeze-dried for 2 hours.

Doctor-blade coating of HNM

An immobilized 90°-beveled razor blade (Fisher, 10 cm wide) was gently placed on the substrate. The GO/HCS weight ratio used was 1:1. One microliter of the GO/HCS composite suspension mixture, combined with polyvinylidene fluoride (PVDF) as a binder and *N*-methyl-2-pyrrolidone (NMP) as a solvent, was dispensed along the side wall of the blade and onto the substrate. The blade was dragged by a syringe pump at a controlled 0.2 m/min; the blade could then spread the colloidal suspension uniformly on the substrate.

Characterization methods

Scanning electron microscopy

For the preparation of SEM samples, 3 to 5 mg of the samples to be tested were collected and evenly dispersed on a conductive adhesive on the sample stage. The sample was treated by gold sputter coating for 40 s. In this study, a Quanta2000 SEM manufactured by the U.S. FEI Company was used to characterize the samples' microscopic morphology.

Determination of the surface area and pore structure

This study adopted an automatic sorption analyzer to determine the surface area and pore structure parameters of the carbon spheres. Nitrogen was used as the adsorption medium at 77 K, and the adsorption isotherms were measured in the relative pressure range of 0.01 to 0.9. Before testing, the sample was vented for 5 hours in a vacuum environment at 300°C. The adsorption capacity of the sample was calculated using the multipoint BET (*22*) equation. The micropore volume and surface area were calculated according to the *t*-plot method. The pore size distribution was determined using a density functional theory (*35*) model.

Fourier transform IR and Raman spectroscopy

Fourier transform IR (FTIR) spectroscopy was used to determine the types of functional groups on the surface of the carbon spheres. Samples were subjected to IR spectroscopy analysis using a Nicolet FTIR spectrometer. First, 5 mg of carbon spheres and HCS were placed in an agate mortar, and high-purity KBr was added. After the mixture was fully ground, the sample was pressed into a transparent sheet by a tablet machine and placed in an IR spectrometer for measurement. For measurement conditions, the sample was scanned 60 times with a resolution of 2 cm^{-1} over the scanning range of 400 to 4000 cm^{-1}. Raman spectra were recorded with a Jobin-Yvon HR800 Raman spectrometer with 632.8-nm wavelength incident laser light.

XRD analysis

A Siemens D8 Advance ECO (Bruker, USA) x-ray diffractometer was used with a Cu Ka radiation source with a wavelength of 0.15 nm. The tube voltage was 40 kV, the tube current was 30 mA, the angle scan rate was 1°/min, and the scan step was 0.02°. The XRD patterns were used to analyze changes in the internal crystal structure of cellulose after heating.

Adsorption experiments

The adsorption isotherms were performed gravimetrically using a sorption analyzer (TA Instruments, model VTI-SA) at 298 K with N_2 as the carrier gas. The system logged the equilibrium weight of the biomass-based hierarchical porous carbon in response to a step change in the concentration of the adsorbate (relative pressure range of 0.01 to 0.9). Between 3 and 5 mg of hierarchical porous carbon powder was weighed and placed into the analyzer. Equilibrium was assumed to be reached when the weight changed by less than 0.001% in 5 min.

To conduct the low-concentration adsorption experiment, a distinct apparatus was used, which is shown schematically in Fig. 6A. During the adsorption process, the toluene/acetone vapor was generated and controlled with a 100-ml (Hamilton) syringe pump (KD Scientific, model 200). A three-way valve with a photoionization detector (RAE Systems, MiniRAE 2000) was set to continuously determine the inlet concentration before N_2 was mixed with toluene/acetone and fed into the HNM. All experiments were conducted at an initial concentration of 200 ppmv of toluene/acetone. The outlet concentration was recorded every 15 min until the outlet gas concentration was stabilized at 99% of the inlet concentration.

H_2 isotherms at 77 K at low pressure (0 to 1.2 bar) were measured in liquid nitrogen and liquid argon baths, respectively. Oil-free vacuum pumps and oil-free pressure regulators were used for measurements.

SUPPLEMENTARY MATERIALS

Supplementary material for this article is available at http://advances.sciencemag.org/cgi/content/full/6/41/eabb0694/DC1

REFERENCES AND NOTES

1. W. Liu, S.-D. Jiang, Y. Yan, W. Wang, J. Li, K. Leng, S. Japip, J. Liu, H. Xu, Y. Liu, I.-H. Park, Y. Bao, W. Yu, M. D. Guiver, S. Zhang, K. P. Loh, A solution-processable and ultra-permeable conjugated microporous thermoset for selective hydrogen separation. *Nat. Commun.* **11**, 1633 (2020).
2. J. Liu, N. P. Wickramaratne, S. Z. Qiao, M. Jaroniec, Molecular-based design and emerging applications of nanoporous carbon spheres. *Nat. Mater.* **14**, 763–774 (2015).
3. X. Xie, C. Chen, N. Zhang, Z.-R. Tang, J. Jiang, Y.-J. Xu, Microstructure and surface control of MXene films for water purification. *Nat. Sustain.* **2**, 856–862 (2019).
4. S. Yi, B. Ghanem, Y. Liu, I. Pinnau, W. J. Koros, Ultraselective glassy polymer membranes with unprecedented performance for energy-efficient sour gas separation. *Sci. Adv.* **5**, eaaw5459 (2019).
5. P. Li, J. Li, X. Feng, J. Li, Y. Hao, J. Zhang, H. Wang, A. Yin, J. Zhou, X. Ma, B. Wang, Metal-organic frameworks with photocatalytic bactericidal activity for integrated air cleaning. *Nat. Commun.* **10**, 2177 (2019).
6. J. E. Bachman, Z. P. Smith, T. Li, T. Xu, J. R. Long, Enhanced ethylene separation and plasticization resistance in polymer membranes incorporating metal–organic framework nanocrystals. *Nat. Mater.* **15**, 845–849 (2016).
7. M. Y. Jeon, D. Kim, P. Kumar, P. S. Lee, N. Rangnekar, P. Bai, M. Shete, B. Elyassi, H. S. Lee, K. Narasimharao, S. N. Basahel, S. Al-Thabaiti, W. Xu, H. J. Cho, E. O. Fetisov, R. Thyagarajan, R. F. Dejaco, W. Fan, K. A. Mkhoyan, J. I. Siepmann, M. Tsapatsis, Ultra-selective high-flux membranes from directly synthesized zeolite nanosheets. *Nature* **543**, 690–694 (2017).
8. L.-H. Xie, X.-M. Liu, T. He, J.-R. Li, Metal-organic frameworks for the capture of trace aromatic volatile organic compounds. *Chem* **4**, 1911–1927 (2018).
9. E. Y. Lee, M. P. Suh, A robust porous material constructed of linear coordination polymer chains: Reversible single-crystal to single-crystal transformations upon dehydration and rehydration. *Angew. Chem. Int. Ed.* **43**, 2798–2801 (2004).
10. J. Abraham, K. S. Vasu, C. D. Williams, K. Gopinadhan, Y. Su, C. T. Cherian, J. Dix, E. Prestat, S. J. Haigh, I. V. Grigorieva, P. Carbone, A. K. Geim, R. R. Nair, Tunable sieving of ions using graphene oxide membranes. *Nat. Nanotechnol.* **12**, 546–550 (2017).
11. J. Zhao, G. Zhou, K. Yan, J. Xie, Y. Li, L. Liao, Y. Jin, K. Liu, P.-C. Hsu, J. Wang, H.-M. Cheng, Y. Cui, Air-stable and freestanding lithium alloy/graphene foil as an alternative to lithium metal anodes. *Nat. Nanotechnol.* **12**, 993–999 (2017).
12. S. Wang, D. Mahalingam, B. Sutisna, S. P. Nunes, 2D-dual-spacing channel membranes for high performance organic solvent nanofiltration. *J. Mater. Chem. A* **7**, 11673–11682 (2019).
13. B. Lu, X. Yuan, Y. Ren, Q. Shi, S. Wang, J. Dong, Z.-d. Nan, Cost-effective three dimensional Ag/polymer dyes/graphene-carbon spheres hybrids for high performance nonenzymatic sensor and its application in living cell H_2O_2 detection. *Bioelectrochemistry* **123**, 103–111 (2018).
14. X. Zheng, G. Shen, C. Wang, Y. Li, D. Dunphy, T. Hasan, C. J. Brinker, B.-L. Su, Bio-inspired Murray materials for mass transfer and activity. *Nat. Commun.* **8**, 14921 (2017).
15. C. Falco, N. Baccile, M.-M. Titirici, Morphological and structural differences between glucose, cellulose and lignocellulosic biomass derived hydrothermal carbons. *Green Chem.* **13**, 3273–3281 (2011).
16. R. Li, A. Shahbazi, A review of hydrothermal carbonization of carbohydrates for carbon spheres preparation. *Trends Renew. Energ.* **1**, 43–56 (2015).
17. Y. Mi, W. Hu, Y. Dan, Y. Liu, Synthesis of carbon micro-spheres by a glucose hydrothermal method. *Mater. Lett.* **62**, 1194–1196 (2008).
18. T. Li, S. X. Li, W. Kong, C. Chen, E. Hitz, C. Jia, J. Dai, X. Zhang, R. Briber, Z. Siwy, M. Reed, L. Hu, A nanofluidic ion regulation membrane with aligned cellulose nanofibers. *Sci. Adv.* **5**, eaau4238 (2019).
19. M. Sevilla, A. B. Fuertes, The production of carbon materials by hydrothermal carbonization of cellulose. *Carbon* **47**, 2281–2289 (2009).
20. S. Brunauer, L. S. Deming, W. E. Deming, E. Teller, On a theory of the van der waals adsorption of gases. *J. Am. Chem. Soc.* **62**, 1723–1732 (1940).
21. L. Jiang, L. Sheng, C. Long, Z. Fan, Densely packed graphene nanomesh-carbon nanotube hybrid film for ultra-high volumetric performance supercapacitors. *Nano Energy* **11**, 471–480 (2015).

22. S. Brunauer, P. H. Emmett, E. Teller, Adsorption of gases in multimolecular layers. *J. Am. Chem. Soc.* **60**, 309–319 (1938).
23. N. Zhang, N. Gao, C. Fu, D. Liu, S. Li, L. Jiang, H. Zhou, Y. Kuang, Hierarchical porous carbon spheres/graphene composite for supercapacitor with both aqueous solution and ionic liquid. *Electrochim. Acta* **235**, 340–347 (2017).
24. H. Li, K. Wu, J. Lim, H.-J. Song, V. I. Klimov, Doctor-blade deposition of quantum dots onto standard window glass for low-loss large-area luminescent solar concentrators. *Nat. Energy* **1**, 16157 (2016).
25. K. Vellingiri, P. Kumar, A. Deep, K.-H. Kim, Metal-organic frameworks for the adsorption of gaseous toluene under ambient temperature and pressure. *Chem. Eng. J.* **307**, 1116–1126 (2017).
26. H. Irvani, M. Pour, A. Vahidi, S. Arezoomandan, H. S.-F. Abady, Removal of toluene vapors from the polluted air with modified natural zeolite and titanium dioxide nanoparticles. *Med. Gas Res.* **8**, 91–97 (2018).
27. M. A. Lillo-Ródenas, D. Cazorla-Amorós, A. Linares-Solano, Behaviour of activated carbons with different pore size distributions and surface oxygen groups for benzene and toluene adsorption at low concentrations. *Carbon* **43**, 1758–1767 (2005).
28. H. Wang, S. Min, C. Ma, Z. Liu, W. Zhang, Q. Wang, D. Li, Y. Li, S. Turner, Y. Han, H. Zhu, E. Abou-Hamad, M. N. Hedhili, J. Pan, W. Yu, K.-W. Huang, L.-J. Li, J. Yuan, M. Antonietti, T. Wu, Synthesis of single-crystal-like nanoporous carbon membranes and their application in overall water splitting. *Nat. Commun.* **8**, 13592 (2017).
29. F. Xu, Z. Tang, S. Huang, L. Chen, Y. Liang, W. Mai, H. Zhong, R. Fu, D. Wu, Facile synthesis of ultrahigh-surface-area hollow carbon nanospheres for enhanced adsorption and energy storage. *Nat. Commun.* **6**, 7221 (2015).
30. C. Buttersack, Modeling of type IV and V sigmoidal adsorption isotherms. *Phys. Chem. Chem. Phys.* **21**, 5614–5626 (2019).
31. R. Li, S. Chong, N. Altaf, Y. Gao, B. Louis, Q. Wang, Synthesis of ZSM-5/siliceous zeolite composites for improvement of hydrophobic adsorption of volatile organic compounds. *Front. Chem.* **7**, 505 (2019).
32. M. Baca, K. Cendrowski, P. Banach, B. Michalkiewicz, E. Mijowska, R. J. Kalenczuk, Effect of Pd loading on hydrogen storage properties of disordered mesoporous hollow carbon spheres. *Int. J. Hydrogen Energy* **42**, 30461–30469 (2017).
33. D. J. Levine, T. Runčevski, M. T. Kapelewski, B. K. Keitz, J. Oktawiec, D. A. Reed, J. A. Mason, H. Z. H. Jiang, K. A. Colwell, C. M. Legendre, S. A. Fitzgerald, J. R. Long, Olsalazine-based metal-organic frameworks as biocompatible platforms for H_2 adsorption and drug delivery. *J. Am. Chem. Soc.* **138**, 10143–10150 (2016).
34. V. Abdelsayed, S. Moussa, H. M. Hassan, H. S. Aluri, M. M. Collinson, M. S. El-Shall, Photothermal deoxygenation of graphite oxide with laser excitation in solution and graphene-aided increase in water temperature. *J. Phys. Chem. Lett.* **1**, 2804–2809 (2010).
35. T. Munakata, Density functional theory and langevin-diffusion equation. *Strongly Coupled Plasma Phys.* **1990**, 695–698 (1990).
36. I. I. Laskar, Z. Hashisho, Insights into modeling adsorption equilibria of single and multicomponent systems of organic and water vapors. *Sep. Purif. Technol.* **241**, 116681 (2020).

Acknowledgments

Funding: This work was supported as part of the Center for Gas Separations Relevant to Clean Energy Technologies, an Energy Frontier Research Center funded by the United States. This work was supported by the U.S. Department of Energy (DOE), Office of Basic Energy Sciences, Division of Materials Sciences and Engineering (contract no. DE-AC02-76SF00515). D.M.H. acknowledges support from the Joint Center for Energy Storage Research, an Energy Innovation Hub funded by the U.S. Department of Energy, Office of Science, Basic Energy Sciences. **Author contributions:** J.A.R. and Y.C. supervised the project. Y.C., J.A.R., J.T., and H.M., conceived the idea, designed the experiments, and cowrote the paper. H.M., J.T., J.C., J.W., K.H., Y.P., D.M.H., L.X., R.Z., X.L., and A.Y. conducted the experiments. All the authors reviewed and commented on the manuscript. **Competing interests:** The authors declare that they have no competing interests. **Data and materials availability:** All data needed to evaluate the conclusions in the paper are present in the paper and/or the Supplementary Materials. Additional data related to this paper may be requested from the authors.

Submitted 28 January 2020
Accepted 21 August 2020
Published 7 October 2020
10.1126/sciadv.abb0694

Citation: H. Mao, J. Tang, J. Chen, J. Wan, K. Hou, Y. Peng, D. M. Halat, L. Xiao, R. Zhang, X. Lv, A. Yang, Y. Cui, J. A. Reimer, Designing hierarchical nanoporous membranes for highly efficient gas adsorption and storage. *Sci. Adv.* **6**, eabb0694 (2020).

ScienceAdvances

Designing hierarchical nanoporous membranes for highly efficient gas adsorption and storage

Haiyan Mao, Jing Tang, Jun Chen, Jiayu Wan, Kaipeng Hou, Yucan Peng, David M. Halat, Liangang Xiao, Rufan Zhang, Xudong Lv, Ankun Yang, Yi Cui, and Jeffrey A. Reimer

Sci. Adv. **6** (41), eabb0694. DOI: 10.1126/sciadv.abb0694